Formation of magnetic discontinuities through viscous relaxation

Sanjay Kumar[1], R. Bhattacharyya[1], and P. K. Smolarkiewicz[2]

[1] *Udaipur Solar Observatory, Physical Research Laboratory,*

Dewali, Bari Road, Udaipur-313001, India and

[2] *European Centre for Medium-Range Weather Forecasts, Reading RG2 9AX, UK.*

(Dated: April 7, 2014)

Abstract

According to Parker's magnetostatic theorem, tangential discontinuities in magnetic field, or current sheets (CSs), are generally unavoidable in an equilibrium magnetofluid with infinite electrical conductivity and complex magnetic topology. These CSs are due to a failure of a magnetic field in achieving force-balance everywhere and preserving its topology while remaining in a spatially continuous state. A recent work [Kumar, Bhattacharyya, and Smolarkiewicz, Phys. Plasmas **20**, 112903 (2013)] demonstrated this CS formation utilizing numerical simulations in terms of the vector magnetic field. The magnetohydrodynamic simulations presented here complement the above work by demonstrating CS formation by employing a novel approach of describing the magnetofluid evolution in terms of magnetic flux surfaces instead of the vector magnetic field. The magnetic flux surfaces being the possible sites on which CSs develop, this approach provides a direct visualization of the CS formation, helpful in understanding the governing dynamics. The simulations confirm development of tangential discontinuities through a favorable contortion of magnetic flux surfaces, as the magnetofluid undergoes a topology-preserving viscous relaxation from an initial non-equilibrium state with twisted magnetic field. A crucial finding of this work is in its demonstration of CS formation at spatial locations away from the magnetic nulls.

PACS numbers: 52.25.Xz, 52.30.Cv, 52.35.Vd, 95.30.Qd

Keywords: MHD, Current Sheet, Magnetic flux surface, EULAG

I. INTRODUCTION

A magnetofluid with infinite electrical conductivity evolves with magnetic field lines being tied to the fluid parcels – referred to as the flux freezing or frozen-in condition. As a consequence, the magnetic flux across an arbitrary fluid surface [1], physically identified by the material elements lying on it, remains conserved in time. Depending on the topology of magnetic field, a subset Γ of fluid surfaces can be identified such that the loci of magnetic field lines are entirely contained on the Γ which, in literature are termed as magnetic flux surfaces (MFSs). It is then imperative that the magnetic flux through a MFS is zero. Under the condition of flux-freezing, the magnetic field lines are tied to the material elements identifying Γ and hence MFS are also valid fluid surfaces. This validity holds only under the condition of flux-freezing and any evolving magnetofluid must maintain it at every instant till a violation of the condition.

To focus on ideas, let us consider a volume of magnetofluid as a stack of MFSs, albeit of complex geometry. In an evolving magnetofluid, these flux surfaces are expected to contort non-uniformly in response to an unbalanced force and result in deforming magnetic field lines lying on the surface. With favorable contortions, a physical scenario is possible where two portions of a given MFS or two entirely different MFSs come arbitrarily close to each other by squeezing out the interstitial fluid so that an infinitesimally small resistivity can become significant. Under this circumstance, the magnetic field may become discontinuous depending on the relative orientation of magnetic field lines lying on the approaching surfaces. From Ampere's law then a current sheet (CS) develops which is an enhanced volume-current density localized at the surface across which the magnetic field is discontinuous.

The above rationale of CS formation is in conformity with the optical analogy of magnetic field lines proposed by Parker [2–5]. In its skeletal form, the analogy uses the similarity in field line equations on a flux surface S of a potential (and hence untwisted) field $\mathbf{B}_p$ with the optical ray paths in a medium of refractive index $\mid \mathbf{B}_p \mid$. The streaming of field lines on S then follows Fermat's principle, resulting in deflection of field lines concavely towards a sufficiently local maximum in $\mid \mathbf{B}_p \mid$. Such deflections in a bunch of field lines then generates a hole on the flux surface co-located to the region where $\mid \mathbf{B}_p \mid \approx \mid \mathbf{B}_p \mid_{max}$. In a general scenario of many such contorting flux surfaces, two MFSs adjacent to the surface S can get

contorted in such a way that the corresponding deformed field lines can intrude through the hole. These intruding field lines being in general not parallel, a formation of CS is inevitable at the contact.

An extension of the optical analogy to twisted magnetic fields [5, 6] is straightforward and, provides a framework on which the computations presented in this work are based. This extension uses a representation of a twisted magnetic field $\mathbf{B}$ in terms of superposing untwisted component fields $\mathbf{B}_i$ [7]. Each of these component fields then can be expressed in terms of a pair of Euler Potentials (EPs) (ψ_i, ϕ_i) [8, 9]. In equation form,

$$\mathbf{B} = \sum_i \mathbf{B}_i = \sum_i W_i(\psi_i, \phi_i) \nabla\psi_i \times \nabla\phi_i \quad , \tag{1}$$

where the index i specifies a component field with magnitude W_i. Both $\psi_i = $ const. and $\phi_i = $ const. surfaces are also global magnetic flux surfaces of the component field $\mathbf{B}_i$, since $\mathbf{B}_i \cdot \nabla\psi_i = \mathbf{B}_i \cdot \nabla\phi_i = 0$. The magnetic field lines being the lines of intersection of the two surfaces, the magnetic topology is determined by the EPs. The optical analogy is then applicable to each of the component fields with their globally defined flux surfaces as pointed out in reference [6]. Further the superposition being linear, a formation of CS on any one of the flux surfaces is expected to enhance the total current density $\mathbf{J} = c/4\pi(\nabla \times \mathbf{B})$. Recognizing the importance of MFSs as described in the optical analogy above, a direct tracking of magnetic flux surface evolution then provides the necessary visualization and hence a better understanding of the inherent dynamics of CS formation.

It is important to note that a global flux surface representation of the twisted field $\mathbf{B}$ is in general not feasible when the field is either periodic or the corresponding field lines are contained wholly within a finite domain. It is then plausible that a single field line may fill up the whole domain [10, 11] and thereby destroy the geometric meanings of the field line as well as the associated flux surfaces [1].

The analytical theory of spontaneous CS formation in a static magnetofluid with infinite electrical conductivity, referred to as the Parker's magnetostatic theorem, was first proposed by Parker [12, 13] and is revisited in reference [14]. The theorem is based on the impossibility of satisfying the two stringent conditions of ideal MHD— the local force balance and the conservation of global magnetic topology as a consequence of flux freezing, with an interlaced magnetic field continuous everywhere. The impossibility in simultaneous satisfaction of these

two constraints of ideal MHD can further be explained in terms of the overdetermined nature of magnetostatic partial differential equations nonlinearly coupled to the integral equations imposing the field topology, and the hyperbolic nature of the torsion coefficient α_0 of a force-free equilibrium characterized by zero Lorentz force [15]. It is further demonstrated by Low [16] that the magnetic topologies of the force-free fields obtainable from an uniform magnetic field through continuous deformation by magnetic footpoint displacements at the end plates of Parker's magnetostatic theorem are a restricted subset of the field topologies similarly created without imposing the force-free condition. The theorem then follows by concluding that a continuous nonequilibrium field with a topology not in this subset must relax to a terminal state containing magnetic discontinuities.

The above discussions then yield a salient point. A successful numerical demonstration of CS formation in an evolving magnetofluid must satisfy the two perquisite conditions; invariance of magnetic topology as a consequence of flux freezing, and the local force-balance obtained in a terminal state of the evolution. The invariance of magnetic topology is a condition which is to be imposed by a proper choice of numerical model whereas the condition of local force balance can be realized by allowing the magnetofluid to relax strictly through viscous dissipation of kinetic energy at the expanse of a finite magnetic energy which has a lower bound fixed by the field topology. To elaborate further, we consider an infinitely conducting, incompressible, and viscous magnetofluid which is described by the MHD Navier-Stokes equations

$$\rho_0 \left(\frac{\partial \mathbf{v}}{\partial t} + (\mathbf{v} \cdot \nabla)\, \mathbf{v} \right) = \mu_0 \nabla^2 \mathbf{v} + \frac{1}{4\pi} (\nabla \times \mathbf{B}) \times \mathbf{B} - \nabla p, \tag{2}$$

$$\nabla \cdot \mathbf{v} = 0, \tag{3}$$

$$\frac{\partial \mathbf{B}}{\partial t} = \nabla \times (\mathbf{v} \times \mathbf{B}), \tag{4}$$

$$\nabla \cdot \mathbf{B} = 0, \tag{5}$$

in standard notations, where ρ_0 and μ_0 are uniform density and coefficient of viscosity respectively. We focus only on the systems periodic in all three Cartesian coordinates. From an initial nonequilibrium state, this magnetofluid would relax towards a terminal state by converting magnetic energy W_M to kinetic energy W_K through equations

$$\frac{dW_K}{dt} = \int \frac{1}{4\pi} \left[(\nabla \times \mathbf{B}) \times \mathbf{B} \right] \cdot \mathbf{v} \; d^3x - \int \mu_0 \left| \nabla \times \mathbf{v} \right|^2 \; d^3x \quad , \tag{6}$$

$$\frac{dW_M}{dt} = - \int \frac{1}{4\pi} \left[(\nabla \times \mathbf{B}) \times \mathbf{B} \right] \cdot \mathbf{v} \; d^3x \quad , \tag{7}$$

$$\frac{dW_T}{dt} = - \int \mu_0 \left| \nabla \times \mathbf{v} \right|^2 \; d^3x \quad , \tag{8}$$

the integrals being over a full period. The Lorentz force being conservative, the irrecoverable loss of kinetic energy is due to viscous dissipation only. The terminal relaxed state is then expected to be in magnetostatic equilibrium as the magnetic field cannot decay to zero because of the flux freezing. Since in absence of magnetic diffusivity the terminal relaxed state is identical in magnetic topology to the initial state; Parker's magnetostatic theorem predicts development of CSs in the terminal state if the initial magnetic field is topologically complex. The importance of viscous relaxation then amounts to providing a local force-balance in a magnetofluid evolving with invariant magnetic topology.

Although introduced here as a mathematical requirement to demonstrate CS formation, a viscous relaxation is also physically realizable depending on the ratio of fluid Reynolds number ($R_F \approx VL/\mu$) to magnetic Reynolds number ($R_M \approx VL/\eta$), where L and V length and speed characteristic to the system. For instance, in solar corona $R_F \approx 10$ in comparison to $R_M \approx 10^{10}$ [17] opening up the possibility of a dominant viscous drag at scales larger than the scales where magnetic diffusion is effective. Other examples where the ratio of viscous to resistive dissipation is of the order of unity or more, can be found in a variety of circumstances related to stellar and galactic plasmas [5].

The possibility of CS formation through a viscous relaxation have already been demonstrated in two recent numerical experiments [1, 6], referred hereafter as NE1 and NE2 respectively. Although conceptually the same, the two experiments utilize two different numerical approaches. In NE1, the initial magnetic field is represented in terms of two intersecting families of global MFSs each of which is a level surface defined by a constant Euler potential (EP). The advantage of NE1 is then in its advection of MFSs instead of magnetic field, leading to simpler equations along with elimination of post-processing errors in determining magnetic topology. An apt trade-off for this advantage is the choice of an untwisted magnetic field to construct the relevant initial value problems (IVPs), as only for such fields global MFSs exist [7]. However, the magnetic field in astrophysical plasmas are believed to

be twisted [18] (and references therein). Consequently the NE2 demonstrates CS formation with an initial twisted magnetic field in relevance to general magnetic morphology of the solar corona. For the purpose, NE2 is based on the advection of magnetic field rather than the flux surfaces. The feature common to both NE1 and NE2 is the finding that the CSs develop near the magnetic field reversal layers, or the magnetic nulls, which are the natural sites for magnetic field to become discontinuous.

Against the above backdrop, the motivation of the present paper is to demonstrate CS formations with an initial twisted magnetic field represented in terms of appropriate MFSs constructed by using equation (1). The simulations are performed in an idealized scenario of incompressible magnetofluid with constant viscosity and periodic boundaries. The representation (1) along with flux surface advections, enables a direct visualization and hence a better conceptual understanding of CS formation through contortion of relevant flux surfaces. Most importantly, the comprehensive numerical experiments reported here confirm the development of CSs at locations away from the magnetic nulls and hence support Parker's magnetostatic theorem in its generality.

The paper is organized as follows. The initial value problem (IVP) and the numerical model are discussed in sections II and III while simulation results are presented in section IV. Section V summarizes these results and highlights the key findings of this work.

II. INITIAL VALUE PROBLEM

To develop a relevant initial value problem, we consider the magnetic field $\mathbf{B} = \{B_x, B_y, B_z\}$ where

$$B_x = \sqrt{3}\sin\left(\frac{2\pi}{L}x\right)\cos\left(\frac{2\pi}{L}y\right)\sin\left(\frac{2\pi}{s_0 L}z\right) + \cos\left(\frac{2\pi}{L}x\right)\sin\left(\frac{2\pi}{L}y\right)\cos\left(\frac{2\pi}{s_0 L}z\right), \quad (9)$$

$$B_y = -\sqrt{3}\cos\left(\frac{2\pi}{L}x\right)\sin\left(\frac{2\pi}{L}y\right)\sin\left(\frac{2\pi}{s_0 L}z\right) + \sin\left(\frac{2\pi}{L}x\right)\cos\left(\frac{2\pi}{L}y\right)\cos\left(\frac{2\pi}{s_0 L}z\right), \quad (10)$$

$$B_z = 2s_0\sin\left(\frac{2\pi}{L}x\right)\sin\left(\frac{2\pi}{L}y\right)\sin\left(\frac{2\pi}{s_0 L}z\right), \quad (11)$$

defined in a triply periodic Cartesian domain of horizontal (x and y) extent L and vertical (z) extent $s_0 L$. The factor s_0 is a dimensionless constant and L represent the characteristic length scale of the system. The above choice is based on the understanding that for $s_0 = 1$, $\mathbf{B}$ reduces to a linear force-free field $\mathbf{B}_{lfff}$ satisfying

$$\nabla \times \mathbf{B}_{lfff} = \alpha_0 \mathbf{B}_{lfff} \quad , \tag{12}$$

with $\alpha_0 = (2\pi\sqrt{3})/L$. The parameter α_0 is known to represent magnetic circulation per unit flux [14] and hence is a measure of the twist in magnetic field lines. The Lorentz force exerted by $\mathbf{B}_{lfff}$ is zero and the equilibrium is maintained by a balance between the magnetic tension and the magnetic pressure [19]. The corresponding magnetic topology is complex enough in terms of twisted field lines along with the usual abundance of two-dimensional (2D) magnetic nulls complemented with sparsely located three-dimensional (3D) magnetic nulls [6]. Based on the above understanding, the field $\mathbf{B}$ can be perceived to be obtainable from $\mathbf{B}_{lfff}$ with a scaling factor $s_0 \neq 1$. The Lorentz force exerted by $\mathbf{B}$ is non zero and has the functional form

$$(\mathbf{J} \times \mathbf{B})_x = 4\left(1 - s_0^2\right) \cos\left(\frac{2\pi}{L}x\right) \sin\left(\frac{2\pi}{L}x\right) \sin^2\left(\frac{2\pi}{L}y\right) \sin^2\left(\frac{2\pi}{s_0 L}z\right) \quad , \tag{13}$$

$$(\mathbf{J} \times \mathbf{B})_y = 4\left(1 - s_0^2\right) \sin^2\left(\frac{2\pi}{L}x\right) \sin\left(\frac{2\pi}{L}y\right) \cos\left(\frac{2\pi}{L}y\right) \sin^2\left(\frac{2\pi}{s_0 L}z\right) \quad , \tag{14}$$

$$\begin{aligned}(\mathbf{J} \times \mathbf{B})_z = {} & 2\left(s_0 - \frac{1}{s_0}\right) \sin^2\left(\frac{2\pi}{L}x\right) \cos^2\left(\frac{2\pi}{L}y\right) \sin\left(\frac{2\pi}{s_0 L}z\right) \cos\left(\frac{2\pi}{s_0 L}z\right) \\ & +2\left(s_0 - \frac{1}{s_0}\right) \cos^2\left(\frac{2\pi}{L}x\right) \sin^2\left(\frac{2\pi}{L}y\right) \sin\left(\frac{2\pi}{s_0 L}z\right) \cos\left(\frac{2\pi}{s_0 L}z\right) \quad .\end{aligned} \tag{15}$$

Hereafter, for all computations we set $L = 2\pi$. The modified $\mathbf{B}$ is then $\mathbf{H} = \{H_x, H_y, H_z\}$ where

$$H_x = \sqrt{3} \sin x \cos y \sin\left(\frac{z}{s_0}\right) + \cos x \sin y \cos\left(\frac{z}{s_0}\right) \quad , \tag{16}$$

$$H_y = -\sqrt{3} \cos x \sin y \sin\left(\frac{z}{s_0}\right) + \sin x \cos y \cos\left(\frac{z}{s_0}\right) \quad , \tag{17}$$

$$H_z = 2 s_0 \sin x \sin y \sin\left(\frac{z}{s_0}\right) \quad , \tag{18}$$

defined in the domain of volume $s_0(2\pi)^3$. We use this modified field $\mathbf{H}$ as the initial magnetic field for simulations presented in this paper. The figure 1 illustrates that the maximum amplitude of Lorentz force (solid line) along with magnetic helicity (dashed line) and magnetic energy (dotted line) integrated over the domain volume, increase with s_0. For a comparison with the linear force-free field, the plotted magnetic energy and the helicity are normalized to their corresponding values for $s_0 = 1$. To further quantify this increase we note that a

straightforward calculation yields the domain integrated magnetic energy and the magnetic helicity (K_M) in the following form

$$W_M = 2\pi^2 \left(2 + s_0^2\right) \int_0^{2\pi s_0} dz \ , \tag{19}$$

$$K_M = 2\sqrt{3}\pi^2 s_0 \int_0^{2\pi s_0} dz \ , \tag{20}$$

where the factor s_0 outside the integral sign is contributed by the amplitude of H_z. The limits of the definite integrals indicate further contributions of s_0 to the values of W_M and K_M through the size of the vertical extension. We must point out here that the above calculation of magnetic helicity uses its classical expression

$$K_M = \int \mathbf{A} \cdot \mathbf{H} dV \ , \tag{21}$$

with $\mathbf{A}$ as the vector potential and the integral being over the domain volume. This expression of K_M for a periodic domain, as in our case, is valid only with a constant gauge. A more general gauge independent representation of magnetic helicity along with the involved physics can be found in references [20–22]. In continuation, it is also to be emphasized that the simulations presented here preserve the initial magnetic topology, once fixed by the EPs, by numerical means discussed latter in the paper. Thus, an explicit analysis of magnetic helicity in our simulations is inconsequential, and we do not pursue in this direction further.

For a selection of s_0 appropriate to our simulations, we recall from figure 1 that the initial Lorentz force increases with s_0. The selection criteria is then based on the generation of an initial Lorentz force such that the evolving CSs can be well resolved in time and space with a minimal computational expanse. Based on an auxiliary numerical study, we select $s_0 = 2$ and $s_0 = 3$ for the simulations discussed. The figure 2(a) illustrates the distribution of 2D and 3D magnetic nulls in the computational domain for $s_0 = 3$. In figure 2(b) we have illustrated the same for $s_0 = 1$ to demonstrate the similar spatial distribution of magnetic nulls for the corresponding lfff.

To put our work in general relevance to the contemporary studies of CS formation utilizing stretched magnetic field [14, 23, 24]; we note that the functional form of $\mathbf{H}$ complemented with a vertical extension of $2\pi s_0$ alters the wave number of a Fourier mode in the z-direction by an amount $1/s_0$. For $s_0 > 1$ then, the corresponding wavelength gets elongated by an

amount s_0 in comparison to the same for the lfff characterized by $s_0 = 1$. For a choice of $s_0 > 1$ then,the computational setup presented here inherently couples deepening of the vertical extension to a deviation of $\mathbf{H}$ from its corresponding linear force-free configuration.

To obtain an EP representation of $\mathbf{H}$ utilizing equation (1), we note that an individual component field $\mathbf{H}_i$ has to be untwisted in order to have two intersecting families of global MFSs on which the field lines of $\mathbf{H}_i$ lye. Utililizing this criteria, a valid EP representation of $\mathbf{H}$ can be written with $\mathbf{H} = \sum_{i=1}^{3} \mathbf{H}_i$, where

$$\mathbf{H}_1 = \sqrt{3} \sin x \cos y \sin\left(\frac{z}{s_0}\right) \hat{e}_x - \sqrt{3} \cos x \sin y \sin\left(\frac{z}{s_0}\right) \hat{e}_y \ , \tag{22}$$

$$\mathbf{H}_2 = \cos x \sin y \cos\left(\frac{z}{s_0}\right) \hat{e}_x + s_0 \sin x \sin y \sin\left(\frac{z}{s_0}\right) \hat{e}_z \ , \tag{23}$$

$$\mathbf{H}_3 = \sin x \cos y \cos\left(\frac{z}{s_0}\right) \hat{e}_y + s_0 \sin x \sin y \sin\left(\frac{z}{s_0}\right) \hat{e}_z \ . \tag{24}$$

The component fields $\mathbf{H}_1$, $\mathbf{H}_2$ and $\mathbf{H}_3$ are solenoidal and untwisted, the latter can be verified by noting that $(\nabla \times \mathbf{H}_i) \cdot \mathbf{H}_i = 0$. An EP representation for each component field is then given by

$$\mathbf{H}_i = \nabla\psi_i(x, y, z) \times \nabla\phi_i(x, y, z) \ , \tag{25}$$

where $i = 1, 2, 3$. Once identified, the amplitude of EPs remain invariant in time — as pointed out in reference [1]. The corresponding advection equations are realized by noting that a particular level set of each of the above six EPs can also be identified to fluid surfaces. Once identified, the level sets evolve as fluid surfaces defined by the material elements lying on it and thus satisfy the advection equations

$$\frac{d\psi_i}{dt} = 0 \ , \tag{26}$$

$$\frac{d\phi_i}{dt} = 0 \ , \tag{27}$$

implying

$$\frac{\partial\psi_i}{\partial t} + \mathbf{v} \cdot \nabla\psi_i = 0 \ , \tag{28}$$

$$\frac{\partial\phi_i}{\partial t} + \mathbf{v} \cdot \nabla\phi_i = 0 \ , \tag{29}$$

for $i = 1, 2, 3$. It is understood that an identification of level sets of EPs as fluid surfaces is non-unique but once identified, the above advection equations maintain this identity throughout their evolution under the condition of flux-freezing. For details, the reader is referred to [1]. A suitable EP representation of the initial magnetic field $\mathbf{H}$ is then constructed as

$$\mathbf{H}_1 = \nabla \left(s_0 \sqrt{3} \sin x \sin y \right) \times \nabla \left(- \cos \left(\frac{z}{s_0} \right) \right) \ , \tag{30}$$

$$\mathbf{H}_2 = \nabla \left(s_0 \cos x \sin \left(\frac{z}{s_0} \right) \right) \times \nabla \cos y \ , \tag{31}$$

$$\mathbf{H}_3 = \nabla \left(s_0 \cos y \sin \left(\frac{z}{s_0} \right) \right) \times \nabla \left(- \cos x \right) \ . \tag{32}$$

Figures 3(a), 3(b) and 3(c) illustrate the level sets of the above EPs in pairs — (ψ_1, ϕ_1), (ψ_2, ϕ_2) and (ψ_3, ϕ_3) respectively, with ψ-constant surfaces in color red and ϕ-constant surfaces in color blue, overlaid with field lines (in color green) which are closed curves since the component fields are untwisted. The plots are for $s_0 = 3$. It is straightforward to confirm the existence of a field-reversal layer in $\mathbf{H}_1$ at $z = 3\pi$. Further from figure 3(a), the axes of ψ_1 constant Euler surfaces are lines along the z-direction located at $(x, y) = (\pi/2, \pi/2)$, $(x, y) = (3\pi/2, \pi/2)$, $(x, y) = (\pi/2, 3\pi/2)$ and $(x, y) = (3\pi/2, 3\pi/2)$ respectively. These axes represent O-type neutral lines at which $\mid \mathbf{H}_1 \mid = 0$. Likewise, the other two component fields $\mathbf{H}_2$ and $\mathbf{H}_3$ have field-reversal layers at planes $y = \pi$ and $x = \pi$ respectively. The O-type neutral lines for $\mathbf{H}_2$ are along the y-axis and are located at $(x, z) = (\pi, 3\pi/2)$ and $(x, z) = (\pi, 9\pi/2)$. Whereas, $\mathbf{H}_3$ has O-type neutral lines oriented along the x-direction and is located at $(y, z) = (\pi, 3\pi/2)$ and $(y, z) = (\pi, 9\pi/2)$.

III. NUMERICAL MODEL

A successful numerical demonstration of spontaneous CS formation demands the frozen-in condition to be satisfied with a high fidelity such that the identity of a fluid surface as a magnetic flux surface is maintained to a reasonable accuracy during magnetofluid evolution. The computational requirement is then a minimization of numerically generated dissipation and dispersion errors. If present, these errors destroy the connectivity of the flux surfaces and are thus ambiguous to their evolution in a magnetofluid under flux-freezing. Such a minimization is a signature of a class of inherently nonlinear high-resolution transport methods

that conserve field extrema along flow trajectories while ensuring higher order accuracy away from steep gradients in the advected fields. For our calculations we adapt the MHD version [25] of the well established general-purpose numerical hydrodynamic model EULAG predominantly used in atmospheric and climate research [26, 27]. The model is based entirely on the spatio-temporally second order accurate nonoscillatory forward-in-time (NFT) advection scheme MPDATA (Multidimensional Positive Definite Advection Transport Algorithm) [27].

An important feature of MPDATA relevant to our calculations is its proven effectiveness in performing implicit large-eddy simulations (ILESs) by generating an intermittent and adaptive residual dissipation that mimics the action of explicit subgrid-scale turbulence models whenever the concerned advective field is under-resolved [28]. In a recent work, Ghizaru and coworkers have successfully simulated regular solar cycles [29] while rotational torsional oscillations in a global solar dynamo has been characterized and analyzed utilizing this ILES scheme [30]. The present understanding along with open questions on modeling the solar dynamo are summarized in reference [31]. Furthermore, in the recent work [6] we used this ILES mode to obtain numerically induced magnetic reconnections which decay the developing CSs. In the present work, we utilize this MPDATA generated residual dissipation to provide a computational upper limit of the growth in volume current density for a given fixed grid resolution.

In general, the EULAG model solves inhomogeneous transport equations for either compressible or incompressible flows cast in time-dependent curvilinear coordinates. In Cartesian coordinates, as employed in our case, the inhomogeneous transport PDEs take a simple from

$$\frac{\partial \rho_0 \Psi}{\partial t} + \nabla \cdot (\rho_0 \mathbf{v} \Psi) = \rho_0 R \ , \tag{33}$$

where R is a forcing associated with the specific variable Ψ transported in the flow. For example, this forcing can be attributed to the total of pressure gradient, Lorentz force and viscous drag for the momentum transport. Under the assumption of constant density ρ_0 and the magnetofluid to be thermally homogeneous, the variable Ψ is a generic representation of the three components of velocity and the six EPs representing the magnetic field. Important for the efficacy of integration, the transport of ψ_i and ϕ_i takes the elementary homogeneous form with $R \equiv 0$. Noteworthy, following the experience of [29], the source attributed to the

Lorentz force is evaluated in the conservative form $\propto \nabla \cdot \mathbf{B} \otimes \mathbf{B}$, with the magnetic pressure included into the combined pressure gradient term. This source form due to the Lorentz force lends itself to either centered or upwinding discretizations; with an equivalent outcome in the present study, owing to substantial viscous effects in the Navier-Stokes equation.

An EULAG template algorithm for integrating (33) over time interval δt on a discrete grid $\delta_i \mathbf{x}$ can be compactly written in a functional form

$$\Psi_i^{n+1} = \mathcal{A}_i \left(\Psi^n + 0.5\delta t R^n, \mathbf{v}^{n+1/2}, \rho_o \right) + 0.5\delta t R_i^{n+1} \equiv \widehat{\Psi}_i + 0.5\delta t R_i^{n+1} \ , \tag{34}$$

where Ψ_i^{n+1} is the solution sought at the grid point $(\mathbf{x}_i,\, t^{n+1})$, $\mathcal{A}$ is a second-order-accurate, finite-volume operator representing MPDATA., $\mathbf{v}^{n+1/2}$ is a first-order estimate of the transportive solenoidal velocity at $t + 0.5\delta t$, and $\rho_0 =$ constant in our problem. For inviscid dynamics, all terms at t^{n+1} are lumped into the variable R_i^{n+1}. Because MPDATA is fully second-order-accurate in time and space, solving (34) for the Euler potentials prior to momenta readily provides the $\mathcal{O}(\delta t)^3$ estimates of $\mathbf{B}$, via (25), and of the Lorentz force at t^{n+1}. This considerably simplifies the solution procedure compared to the conventional MHD approach [25], and leads to a fully second-order solution for the governing system while admitting propagation of Alfvén modes with zero amplitude error; cf. [32] for a discussion. By casting the induction equation in terms of the Euler potentials, the only unknown at t^{n+1} on the rhs of (34) is the pressure p^{n+1}, which is obtained by solving (to a round-off error [25, 33]) the discrete elliptic equation generated by the incompressibility (3) discretized consistently with the divergence operator implied by $\mathcal{A}$; see [26] and references therein. When present, the viscous term in R_i^{n+1} is typically approximated to first-order as $\nabla^2 \mathbf{v}^{n+1} = \nabla^2 \mathbf{v}^n + \mathcal{O}(\delta t)$, and included into the explicit counterpart $\widehat{\Psi}_i$ of the template algorithm (34). While this effects in the first-order Euler-forward integral of the viscous forcing in the ode $d\Psi/dt = R$ underlying (33) [32], it is physically inconsequential in our problem, since the analytical requirement for the formation of current sheets is zero resistivity which we approximate by relying on high-resolution properties of MPDATA.

The thinness of developing CSs in every numerical experiment is limited by the grid resolution. In the case of advection of EPs, the CSs are expected to form through contortions of the flux surfaces which eventually produce spatial scales that fall below the fixed grid-resolution. Consequently the MPDATA generated residual magnetic diffusivity breaks the flux-freezing, resulting in reconnection of field lines across the developed CSs; effectively

providing a termination point for the simulations since the identity of flux surfaces to fluid surfaces are preserved only in presence of the frozen-in condition.

IV. RESULTS AND DISCUSSIONS

The simulations are carried out with zero initial velocity, on the $128 \times 128 \times 256$ grid in x, y, and z. Also we provide computational results for two different viscosities $\mu_1 = 0.0075$ and $\mu_2 = 0.0085$, for each s_0.

To obtain an overall understanding of the simulated viscous relaxation, in figure 4 we have plotted the magnetic and kinetic energies normalized to the initial total energy (kinetic + magnetic). The solid and dashed lines in the figures represent evolution with μ_1 and μ_2 respectively. The kinetic energy curves show a sharp rise as the initial Lorentz force pushes the magnetofluid and drives flow at the expanse of magnetic energy. This increase in fluid velocity is arrested by viscosity resulting in the peaks of kinetic energy appearing near $t = 12s$. Subsequently, the magnetofluid relaxes to a quasi-steady phase marked from $t = 64s$ to $t = 144s$ as the magnetic field is depleted of its free energy. This quasi-steady phase is characterized by an almost constant kinetic energy while the change in magnetic energy is restricted to $\approx 20\%$ of its total variation. The higher amplitude of the peak kinetic energy for $s_0 = 3$ compared to that of $s_0 = 2$, for both μ_1 and μ_2, is in agreement with the understanding that the initial Lorentz force increases with s_0 (figure 1).

The formation of CSs are indicative from figures $5(a)$ and $5(b)$ which depict a tendency of rise in volume averaged and maximum total current densities denoted as $<| \mathbf{J} |>$ and $| \mathbf{J} |_{max}$ respectively. To explain the observed non-monotonic rise of $<| \mathbf{J} |>$ and $| \mathbf{J} |_{max}$, in figures $5(c)$, $5(d)$ and $5(e)$ we display evolution of the component current densities $<| \mathbf{J}_1 |>$, $<| \mathbf{J}_2 |>$ and $<| \mathbf{J}_3 |>$ where

$$\mathbf{J}_i = \frac{c}{4\pi} \nabla \times \mathbf{H}_i \tag{35}$$

and,

$$\mathbf{J} = \sum_{i=1}^{3} \mathbf{J}_i \ . \tag{36}$$

for viscosities μ_1 (solid line) and μ_2 (dashed line). Noteworthy is the monotonic increase of all component current densities with time, which attributes the lack of monotonicity in evolution of $<|\ \mathbf{J}\ |>$ and $|\ \mathbf{J}\ |_{max}$ to the possibility of component current densities becoming anti-parallel to each other. Figures $6(a)$ to $6(c)$ depict the relevant cross terms $\mathbf{J}_i \cdot \mathbf{J}_j$ becoming negative in accordance with the above understanding. The plots confirm that till $t = 24s$ the averages $< \mathbf{J}_1 \cdot \mathbf{J}_2 >$, $< \mathbf{J}_1 \cdot \mathbf{J}_3 >$ are almost zero while $< \mathbf{J}_2 \cdot \mathbf{J}_3 >$ is positive and increases with time. Whereas after $t = 24s$, $< \mathbf{J}_1 \cdot \mathbf{J}_2 >$ and $< \mathbf{J}_1 \cdot \mathbf{J}_3 >$ become negative and start decreasing. These negative contributions to the magnitude of total volume current density arrests the monotonic rise resulting in formation of the corresponding peaks in $<|\ \mathbf{J}\ |>$ and $|\ \mathbf{J}\ |_{max}$ at $t = 32s$ and $t = 96s$. Subsequently, from $t = 120s$ onwards the negative contributions from $< \mathbf{J}_1 \cdot \mathbf{J}_2 >$ and $< \mathbf{J}_1 \cdot \mathbf{J}_3 >$ are superseded by other monotonically increasing positive terms – $< \mathbf{J}_2 \cdot \mathbf{J}_3 >$, $<|\ \mathbf{J}_1\ |>$, $<|\ \mathbf{J}_2\ |>$, and $<|\ \mathbf{J}_3\ |>$; resulting in an increase of the maximum and average of total volume current density. The monotonic increase of all the component current densities are in general conformity to formation of CSs in component fields.

To verify computational accuracy, in figure 7 we have plotted the energy budgets for normalized kinetic (solid line) and magnetic (dashed line) energies by calculating the numerical deviations in computed energy balance equations from their analytically correct expressions given by equations (6)-(7) for $\mu = \mu_1$. The plots show the maintenance of this numerical accuracy to be almost precise with a small deviation in kinetic energy balance at $t = 12s$ from its analytically correct value of zero. Noteworthy is the almost accurate maintenance of magnetic energy balance which excludes any possibility of artificially induced magnetic reconnection. From $t = 144s$ onwards the deviations in both magnetic and kinetic energy balance become high and are of the same order. This large deviation in magnetic energy balance points to possible magnetic reconnections mediated via the residual dissipation generated in response to the under-resolved scales. As a consequence, the magnetic topology changes and the EP representation loses its validity since the post-reconnection field lines lye on a different set of EP surfaces. An appreciable numerical deviation in energy budget (for both magnetic and kinetic) after $t = 144s$ (figure 7) then provides a natural termination point for the set of simulations presented here.

To complete the overall understanding, in figure $5(f)$ we have plotted the normalized Lorentz force for μ_1 and μ_2. The plot shows an initial decrease followed by a quasi-steady

phase till $t = 120s$. Subsequently the Lorentz force increases rapidly while being concurrent with the sharp rise in the maximum volume current density.

From the above discussions then the following general picture emerges. The initial Lorentz force pushes the magnetofluid and generates flow by converting magnetic energy into kinetic energy. The monotonic increase in component current densities are supportive to the possibility of CS formation till a threshold in gradient of $\mathbf{H}$ is achieved. In numerical computations presented here, the threshold gradient of developing CSs are provided by the fixed grid resolutions below which the CSs decay through the magnetic reconnection. The plots also show that for a magnetofluid with higher viscosity the CS formation is delayed in time which is in accordance with the general expectation.

Towards a confirmation of CS formation, in figure 8 we display the Direct Volume Rendering (DVR) of $\mid \mathbf{J} \mid$ for computation with viscosity μ_2. The DVR confirms that with a progress in time, the $\mid \mathbf{J} \mid$ becomes more two-dimensional in appearance from its initial three-dimensional structure. Further insight is obtained from the time sequence of magnetic nulls depicted in figure 9 overlaid with a selected isosurface of $\mid \mathbf{J} \mid_{max}$ having an isovalue which is 30% of its maximum value. Hereafter, we refer this isosurface as $J - 30$. The appearance of this surface near $t = 96s$ followed by its spatial extension with time while being concurrent with the increase in $\mid \mathbf{J} \mid_{max}$, is a tell-telling sign of CS formation. An important property of this $J - 30$ surface is in its appearance at spatial locations away from the magnetic nulls. The above finding is further validated by considering other isovalues of $\mid \mathbf{J} \mid_{max}$ but not presented here to minimize the number of figures. This is a key finding of this work since the appearance of CSs away from the magnetic null has already been apprehended by the optical analogy proposed by Parker.

To arrive at a detail understanding of the above finding, in the following we inspect the evolution of EPs along with their corresponding component current densities. For the purpose, in figures 10, 12, and 13 we have displayed the time sequence of EP surfaces: $\phi_1 = 0.25, -0.25$; $\psi_2 = 0.85, -0.85$; and $\phi_2 = -0.40$ overlaid with selected isosurfaces of $\mid \mathbf{J}_1 \mid$ and $\mid \mathbf{J}_2 \mid$ using the nomenclature $J_1 - 60$ and $J_2 - 60$ respectively. Since $\mathbf{J}_1$, $\mathbf{J}_2$ and $\mathbf{J}_3$ are components of $\mathbf{J}$, so the appearance of $J_1 - 60$ and $J_2 - 60$ surfaces (along with $J_3 - 60$ surface) contribute to the development of the $J - 30$ surface. Considering these contributions along with those from the cross terms in $\mid \mathbf{J} \mid$, we have chosen the optimal isovalues for the component current densities to be of 60% of $\mid \mathbf{J} \mid_{max}$. Figure 10 clarifies the

important finding that the appearance of $J_1 - 60$ surface around $t = 96s$ is due to contortion of the ϕ_1 Euler surface. In addition, the $J_1 - 60$ surface is concurrent in time sequence with the development of the $J - 30$ surface. Further, the two sets of surfaces are co-located in the computational domain and have similar structures. This structural similarity along with concurrent and co-located appearance of $J - 30$ and $J_1 - 60$ surfaces ascertain that most of the contribution in $J - 30$ is from $J_1 - 60$. This is in conformity with the observation that the rate of increase of $\mid \mathbf{J}_1 \mid$ is substantially higher than the the same for the other two component current densities. We also note that the contortions of the ϕ_1 Euler surface are spread over the whole MFS and not localized near the intersections with the corresponding O-type neutral line. The cumulative effect of this spread in contortion along with the major contribution of $\mid \mathbf{J} \mid$ coming from $\mid \mathbf{J}_1 \mid$ then culminates into generating CSs in total volume current density that are away from the magnetic nulls.

Further, in figure 11 we present plots of the ϕ_1 Euler surface overlaid with the isosurfaces of $\mid \mathbf{H}_1 \mid$. The panels a and b correspond to instants $t = 48s$ and $t = 128s$ respectively. The isovalue for the $\mid \mathbf{H}_1 \mid$ isosurfaces is chosen to be of 90% of its maximum value at a given instant. As the ϕ_1 Euler surface contorts, oppositely directed field lines come closer resulting in a local increase of the density of field lines and hence the $\mid \mathbf{H}_1 \mid$. In fact, the isovalue for the plotted $\mid \mathbf{H}_1 \mid$ isosurface at $t = 128s$ is almost 3.5 times larger than the same at $t = 48s$. A comparison between the two panels clearly shows a reduction in intersections of the $\mid \mathbf{H}_1 \mid$ isosurfaces with the ϕ_1 Euler surface as it gets more contorted. This reduction in intersections of the two isosurfaces with a concurrent increase of local $\mid \mathbf{H}_1 \mid$ then supports the general understanding that the ϕ_1 Euler surface is more contorted at $t = 128s$ to avoid the zone characterized by an intense $\mid \mathbf{H}_1 \mid$ — a concept essential to the Parker's optical analogy.

The other two component current densities, namely the $\mid \mathbf{J}_2 \mid$ and $\mid \mathbf{J}_3 \mid$, also owe their increase to favorable contortions of the corresponding flux surfaces. Because of such contortions, two sets of $J_2 - 60$ surfaces lying approximately on x-constant and y-constant planes develop as shown in figures 12 and 13. The current surface akin to the x-constant plane is developed by squeezing out the interstitial fluid across the O-type neutral line as displayed in figure 12. While the second current surface identifiable by its approximate orientation similar to a y-constant plane develops from the contortions of the ϕ_2 Euler surfaces (figure 13) across the field reversal layer at $y = \pi$. The time delay between the

appearance of these two sets is due to a combined effect of less contortions in the ϕ_2 Euler surface along with less magnitude of the corresponding component magnetic field and hence, the related current density near the field reversal layer. Similar arguments hold true for an emergence of $J_3 - 60$ surface, the time sequence of which can be visualized through rotating figure 12 by $\pi/2$ along the vertical.

V. SUMMARY

In this work, we have extended our earlier studies [1, 6] to numerically demonstrate CS formation using MFS description of a twisted initial non force-free magnetic field. For the purpose, we have considered the magnetofluid to be incompressible, viscous and having infinite electrical conductivity. The computational domain is of Cartesian geometry with periodic boundaries. From Parker's magnetostatic theorem such CS formation is unavoidable in an equilibrium magnetofluid with interlaced magnetic field lines. To be in conformity with the analytical requirements for generation of CSs, we have utilized a viscous relaxation to obtain a terminal quasi-steady state which is identical in magnetic topology to the initial non-equilibrium state. The initial magnetic field is constructed from a linear force-free field. This construction is based on the understanding that the magnetic topology of the lfff is complex enough in terms of interlaced magnetic field lines and the presence of 2D and 3D nulls. In addition, the lfff is a special solution of a force-free equilibrium which is also realizable in nature. The preservation of the initial magnetic topology is achieved by relying on the second-order-accurate non-oscillatory advection scheme MPDATA. The originality of this work is in its advection of MFSs for the initial non force-free twisted field. The advection of flux surfaces provides the necessary advantage of a direct visualization of evolving flux surfaces providing a better understanding of CS formation.

We also present both indirect and direct evidences of CS formation. The plots of the total average current density and the total maximum current density show tendency to increase with time but also lack monotonicity. We attribute this lack of monotonicity to the flipping of directions in component current densities relative to each other. Realizing the vector nature of $\mathbf{J}$, the observed monotonic increase in every component current density is indicative of CSs formation. It is also found that the process of CSs formation is sensitive to viscosity. For the same initial Lorentz force, the CSs are forming earlier in time for less

viscous magnetofluid as is evident from all the current density plots. This is in agreement with the physical expectation.

A key finding of this work is in its demonstration of CS formation away from the magnetic nulls. The corresponding dynamics is explored by analyzing the evolution of MFSs. The analysis confirms that the MFSs contort in such a way that portions of the same flux surface having oppositely directed field lines come close to each other and thereby increase the gradient of magnetic field. This increased gradient of magnetic field is then responsible for the observed CS formation away from the magnetic nulls.

The computations presented in this paper provide two important insights for a complete interpretation of CS formation in an evolving magnetofluid. First, any parameter related only to the magnitude of volume current density (for example, $\mid \mathbf{J} \mid_{max}$ and $<\mid \mathbf{J} \mid>$) is not a standalone definitive marker to conclude on the possibility of CS formation. In context to our simulations, it is the component current densities that show a monotonic rise whereas the $\mid \mathbf{J} \mid_{max}$ and $<\mid \mathbf{J} \mid>$ develop intermediate peaks. This is expected since a CS formation or the equivalent sharpening of magnetic field gradient is a quality of the vector $\mathbf{J}$ or $\mathbf{H}$ but not its magnitude alone. Second, the CSs may also develop away from the magnetic nulls as apprehended in the optical analogy proposed by Parker. Recognizing the importance of MFSs in the optical analogy, computations utilizing a flux surface representation of magnetic field can be more effective in determining the definitive process through which such CSs develop.

In our case, we find this process to be the contortions of magnetic flux surfaces in a way favorable to CS formation. Additionally, these contortions are found to be in general agreement with Parker's conclusion that streaming magnetic field lines exclude a region where the amplitude of the magnetic field is intense. Such profound insights into the dynamics of CS formation is a novelty associated with computations utilizing advections of appropriate magnetic flux surfaces instead of the magnetic field.

VI. ACKNOWLEDEMENTS

The computations are performed using the High Performance Computing (HPC) cluster at Physical Research Laboratory, India. We also wish to acknowledge the visualisation software VAPOR (www.vapor.ucar.edu), for generating relevant graphics. One of us (PKS)

is supported by funding received from the European Research Council under the European Union's Seventh Framework Programme (FP7/2012/ERC Grant agreement no. 320375). Also, RB wants to thank Dr. B. C. Low for many fruitful discussions during the initiation of this work. The authors also sincerely thank an anonymous reviewer for providing specific suggestions to enhance the presentation as well as to raise the academic content of the paper.

---

[1] R. Bhattacharyya, B.C. Low, and P.K. Smolarkiewicz, Phys. Plasmas **17**, 112901 (2010).

[2] E. N. Parker, Geophys. Astrophys. Fluid Dyn. **45**, 169 (1989).

[3] E. N. Parker, Geophys. Astrophys. Fluid Dyn. **46**, 105 (1989).

[4] E. N. Parker, Geophys. Astrophys. Fluid Dyn. **50**, 229 (1990).

[5] E. N. Parker, *Spontaneous Current Sheets Formation in Magnetic Fields* (Oxford University Press, New York, 1994).

[6] D. Kumar, R. Bhattacharyya, and P. K. Smolarkiewicz, Phys. Plasmas **20**, 112903 (2013).

[7] B. C. Low, Astrophys. J. **649**, 1064 (2006).

[8] D. P. Stern, J. Geophys. Res. **72**, 3995, doi:10.1029/JZ072i015p03995 (1967).

[9] D. P. Stern, Am. J. Phys. **38**, 494 (1970).

[10] J. R. Jokippi and E. N. Parker, Astrophys. J. **155**, 777 (1968).

[11] E. N. Parker, Astrophys. J. **142**, 584 (1965).

[12] E. N. Parker, Astronphys. J. **174**, 499 (1972).

[13] E. N. Parker, Astrophys. J. **330**, 474 (1988).

[14] E. N. Parker, Plasma Phys. Control. Fusion **54**, 124028 (2012).

[15] A. M. Janse, B. C. Low, and E. N. Parker, Phys. Plasmas **17**, 092901 (2010).

[16] B. C. Low, Astrophys. J. **718**, 717 (2010).

[17] M. J. Aschwanden, *Physics of the Solar Corona* (Springer, Berlin, 2004).

[18] D. Kumar and R. Bhattacharyya, Phys. Plasmas **18**, 084506 (2011).

[19] Anrnab Rai Choudhuri, *The Physics of Fluid and Plasmas* (Cambridge Univ. Press, 1999).

[20] M. A. Berger, J. Geophys. Res. **102**, 2637 (1997).

[21] B. C. Low, Phys. Plasmas **18**, 052901 (2011).

[22] R. Bhattacharyya and M. S. Janaki, Phys. Plasmas **11**, 5615 (2004).

[23] A. M. Janse and B. C. Low, Astrophys. J. **690**, 1089 (2009).

[24] D. I. Pontin and Y. -M. Huang, Astrophys. J. **756**, 7 (2012).

[25] P. K. Smolarkiewicz and P. Charbonneau, J. Comput. Phys. **236**, 608 (2013).

[26] J. M. Prusa, P. K. Smolarkiewicz, and A. A. Wyszogrodzki, Comput. Fluids **37**, 1193 (2008).

[27] P. K. Smolarkiewicz, Int. J. Numer. Methods Fluids **50**, 1123 (2006).

[28] L. G. Margolin, W. J. Rider, and F. F. Grinstein, J. Turbul. **7**, N15 (2006).

[29] M. Ghizaru, P. Charbonneau, and P. K. Smolarkiewicz, Astrophys. J. Lett. **715**, L133 (2010).

[30] P. Beaudoin, P. Charbonneau, E. Racine, and P.K. Smolarkiewicz, Sol. Phys. **282**, 335 (2013).

[31] P. Charbonneau and P. K. Smolarkiewicz, Science **340**, 42 (2013).

[32] P. K. Smolarkiewicz and J. Szmelter, J. Comput. Phys. **228**, 33 (2009).

[33] P. K. Smolarkiewicz, V. Grubisic, and L. G. Margolin, Mon. Weather Rev. **125**, 647 (1997).

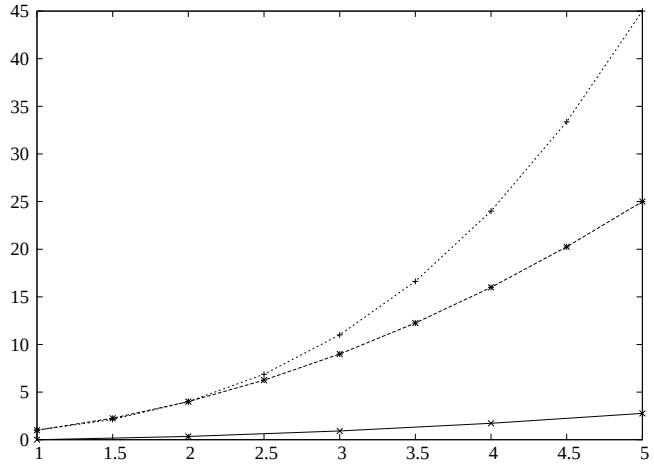

FIG. 1: Variation of magnetic energy (dotted line), magnetic helicity (dashed line) and $|\mathbf{J}\times\mathbf{B}|_{max}$ (solid line) with an increase in s_0. The magnetic energy and the magnetic helicity are normalized to their corresponding values for $s_0 = 1$ (lfff). The plots show an increase in magnetic energy, magnetic helicity and Lorentz force with an increase in s_0.

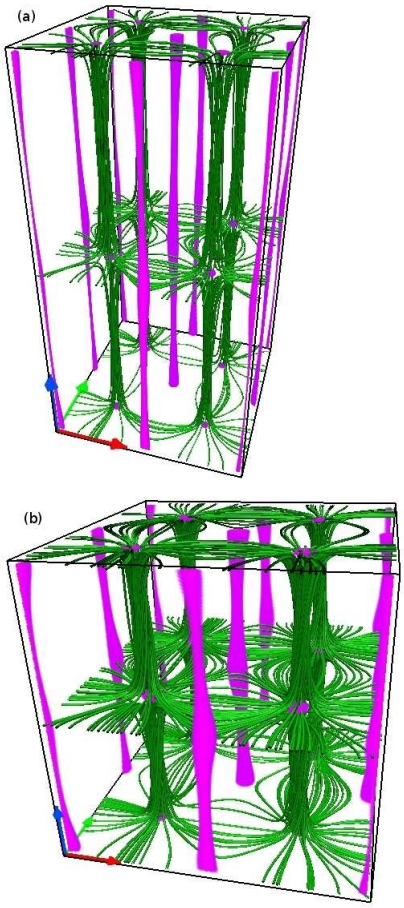

FIG. 2: The panel a illustrates magnetic nulls of the initial field $\mathbf{H}$ for $s_0 = 3$. Panel b shows the same for the corresponding linear force-free field characterized by $s_0 = 1$. The figure depicts the similarity in spatial distribution of magnetic nulls between the lfff and the initial field $\mathbf{H}$.

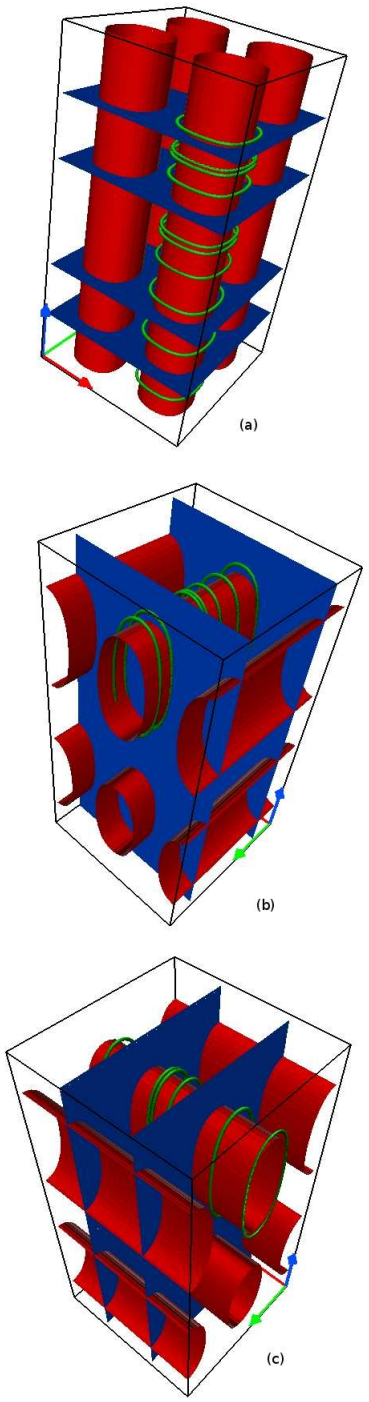

FIG. 3: Panel a depicts the Euler surfaces $\psi_1 = 1.3, -1.3$ (in red); and $\phi_1 = 0.25, -0.25$ (in blue) overlaid with magnetic field lines (in green). Panel b plots the Euler surfaces $\psi_2 = 0.85, -0.85$ (in red); and $\phi_2 = 0.25$ (in blue) with corresponding magnetic field lines (in green). The Euler surfaces $\psi_3 = 0.85, -0.85$ (in red); and $\phi_3 = 0.25$ (in blue) overlaid with field lines (in green) are shown in panel c.

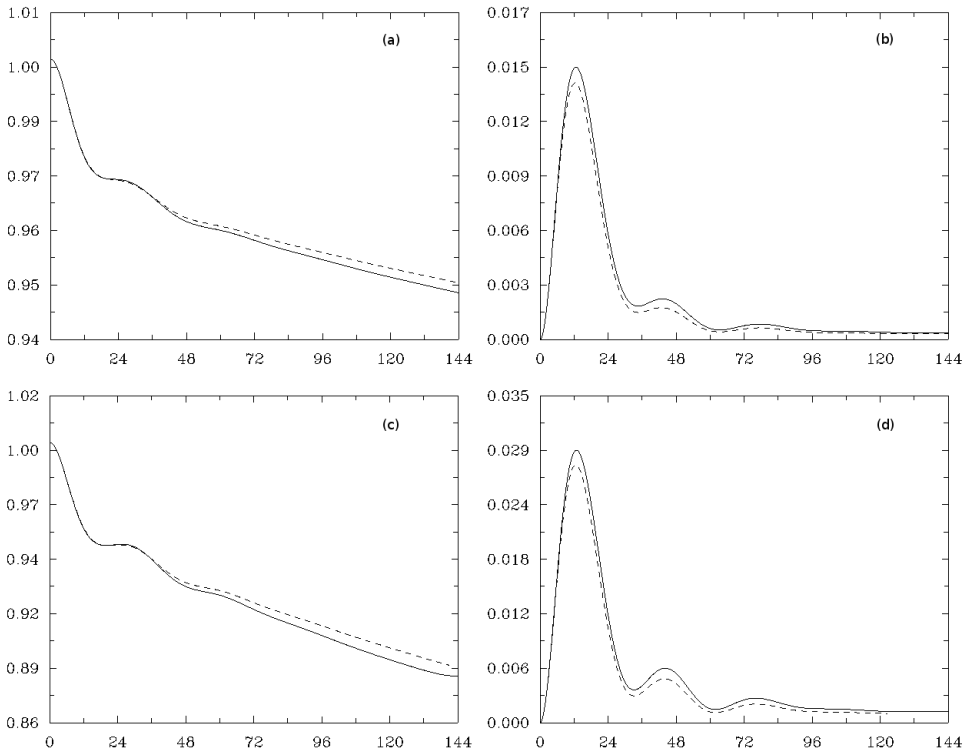

FIG. 4: Time evolution of normalized magnetic and kinetic energies for $s_0 = 2$ (panels a and b) and $s_0 = 3$ (panels c and d). Each plot is for two different viscosities $\mu_1 = 0.0075$ (solid line) and $\mu_2 = 0.0085$ (dashed line). The energies are normalized to the initial total energy. The plots highlight the initial peaks and the quasi-steady phase in kinetic energy. A delayed formation of kinetic energy peak for higher viscosity is in agreement with the general understanding.

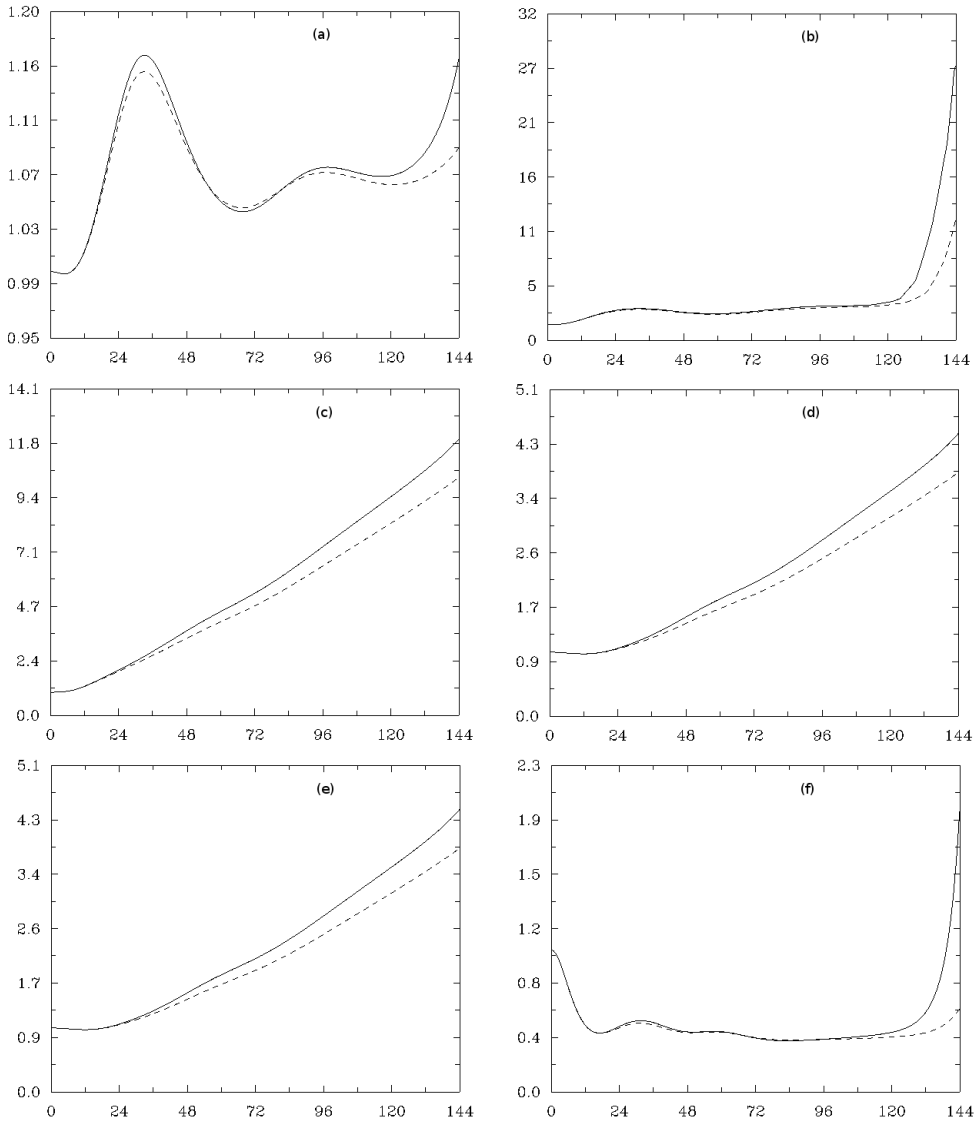

FIG. 5: History of a: $<|\ \mathbf{J}\ |>$, b: $|\ \mathbf{J}_{max}\ |$, c: $<|\ \mathbf{J}_1\ |>$, d: $<|\ \mathbf{J}_2\ |>$, e: $<|\ \mathbf{J}_3\ |>$ and f: grid averaged Lorentz force, for $s_0 = 3$ with viscosities μ_1 (solid lines) and μ_2 (dashed lines); normalized with respect to their initial values. The panels a and b show a lack of monotonicity in evolution of the average and maximum total current density whereas panels c to e depict the component currents increases monotonically.

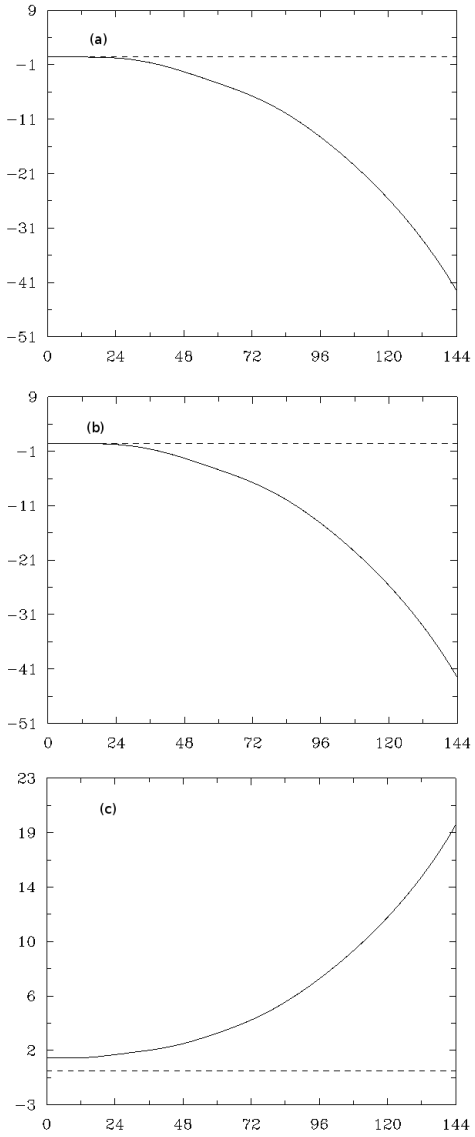

FIG. 6: Time profiles of the normalized a: $< \mathbf{J}_1 \cdot \mathbf{J}_2 >$, b: $< \mathbf{J}_1 \cdot \mathbf{J}_3 >$ and c: $< \mathbf{J}_2 \cdot \mathbf{J}_3 >$ for $s_0 = 3$ and viscosity μ_1; plotted with solid lines. For comparison, zero lines are plotted with dash. The normalization is done with respect to initial value of $< \mathbf{J}_2 \cdot \mathbf{J}_3 >$. The plots exhibit the flipping in direction of component current densities after $t = 24s$.

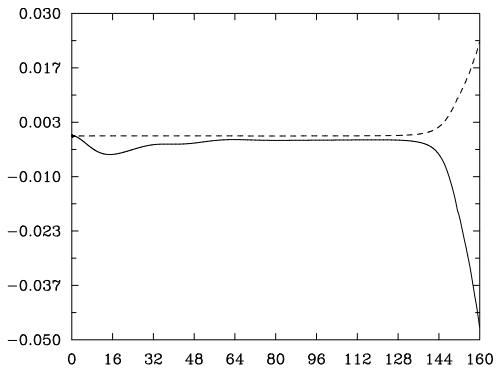

FIG. 7: The history of energy budget for kinetic (solid) and magnetic (dashed) energies for $s_0 = 3$ and viscosity μ_1, normalized to the initial total energy. The plot shows an almost accurate balance in magnetic energy and an acceptable deviation in kinetic energy balance. Both the energy balances are lost at $t = 144s$ onwards and provides a termination point for the simulations.

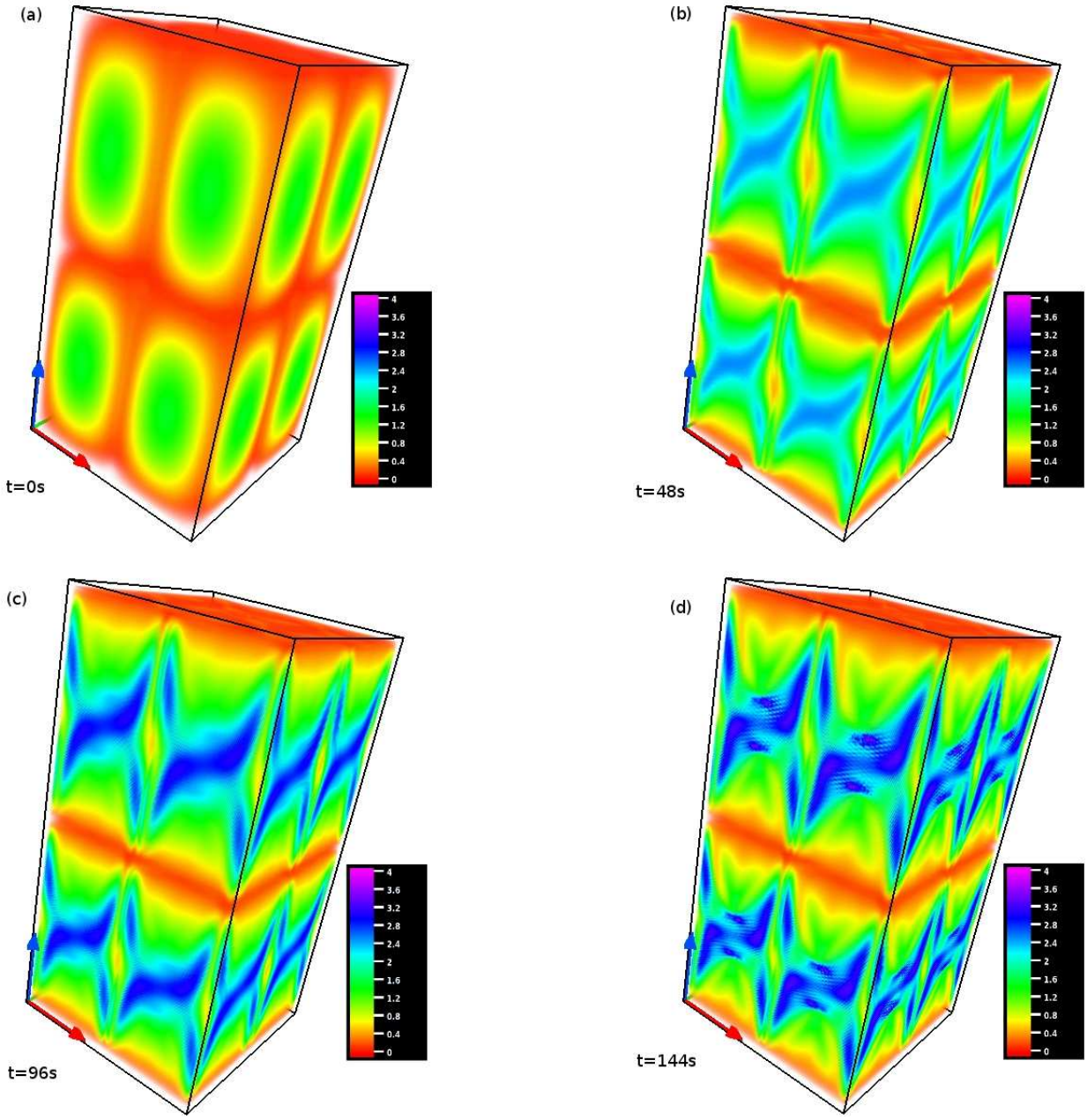

FIG. 8: Time sequence of direct volume rending of total current density $\mid \mathbf{J} \mid$ for $s_0 = 3$ with viscosity μ_2. The figure highlights the appearances of higher values of total current density becoming localized and two dimensional in structure, from an initially three dimensional non-localized form.

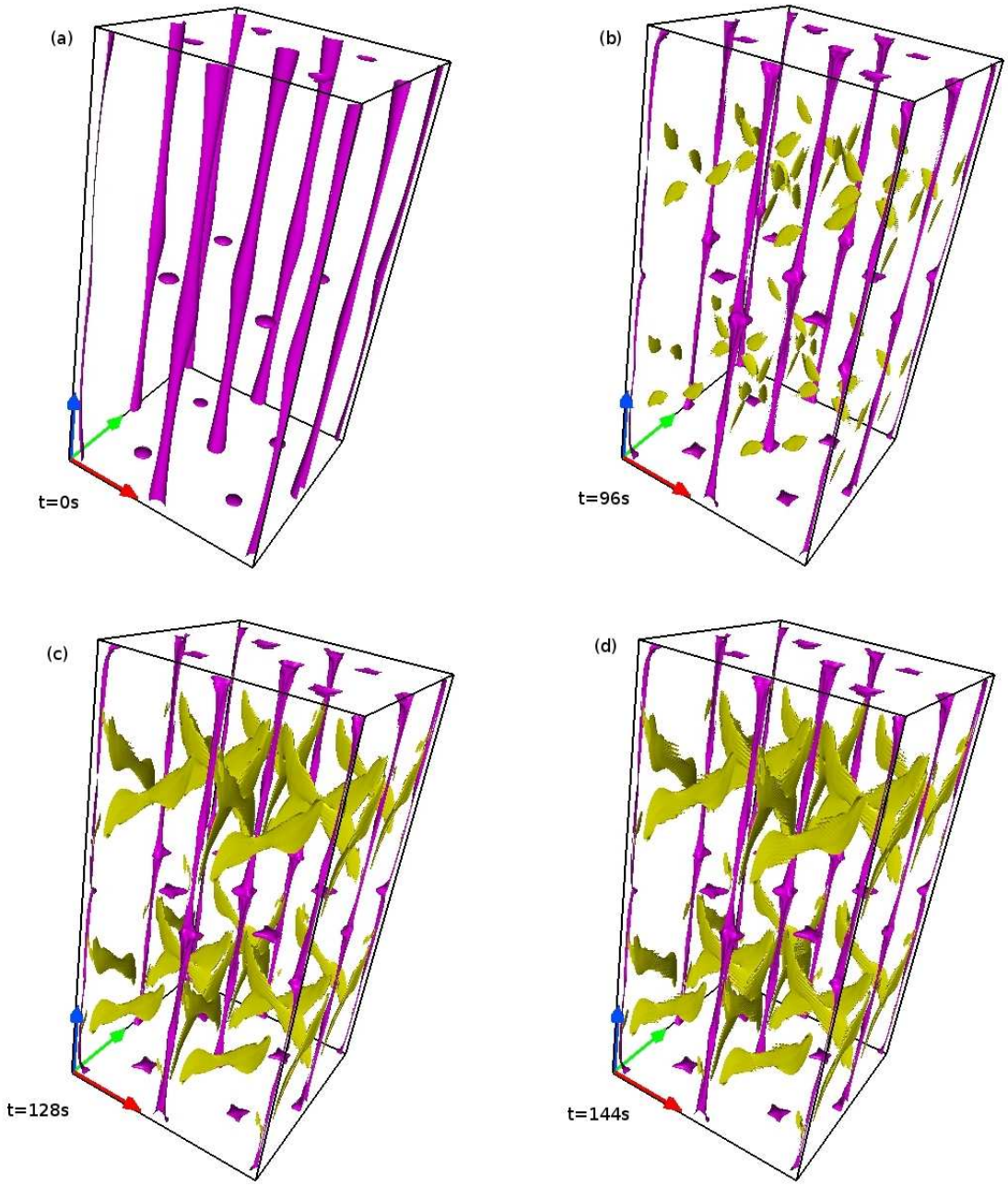

FIG. 9: Time evolution of magnetic nulls (in pink), overlaid with isosurface (in yellow) of total current density having a magnitude of 30% of its maximum value (J-30). The figure illustrates the spatial locations in computational domain where the CSs are forming. Noteworthy is the development of CS away from the magnetic nulls where they are generally expected. Also the topology of the initial magnetic field in terms of spatial distribution of magnetic nulls is preserved throughout the time sequence.

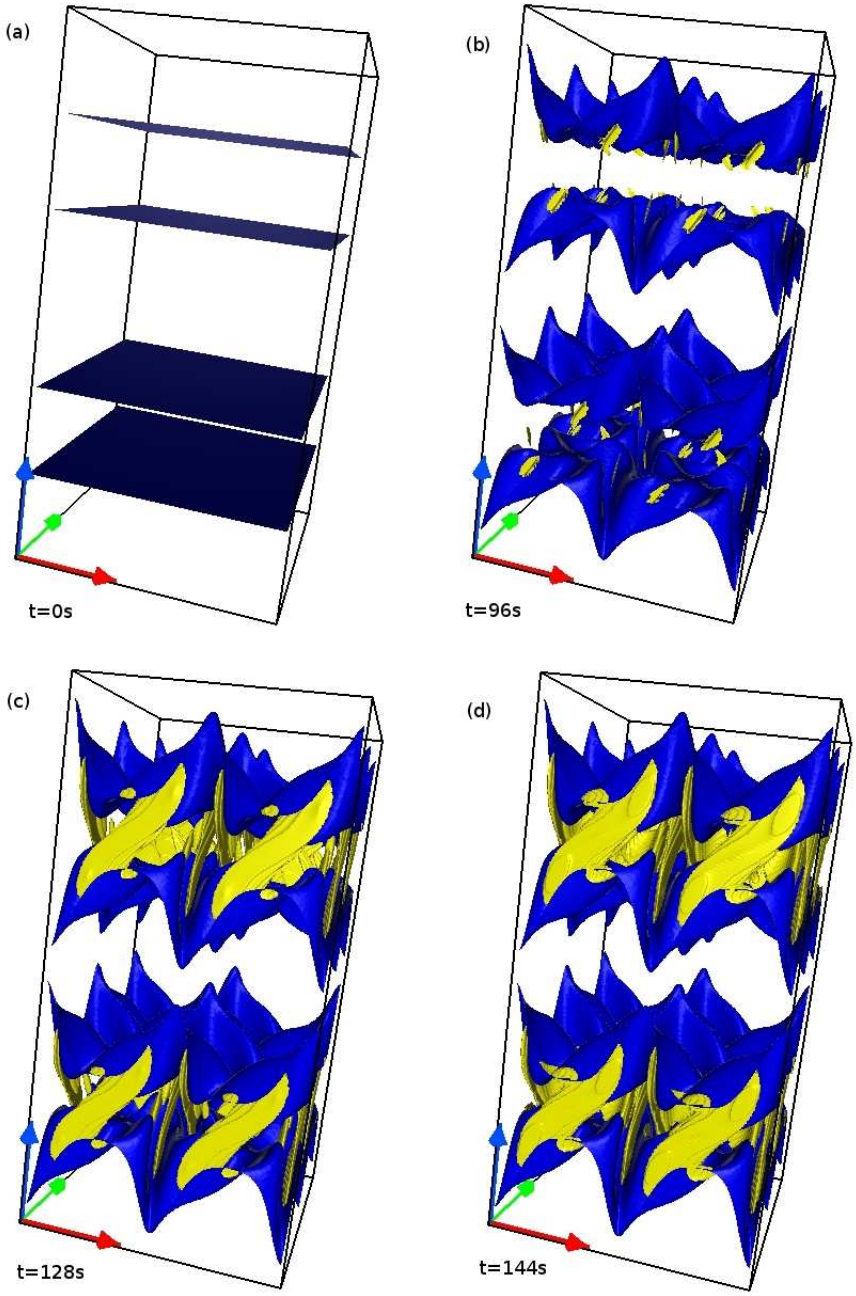

FIG. 10: Evolution of Euler surfaces $\phi_1 = 0.25, -0.25$ (in blue), overlaid with $J_1 - 60$ surface (in yellow). The appearance of $J_1 - 60$ surface are co-located to a contortion of ϕ_1 favorable to bring two oppositely directed field lines towards each other.

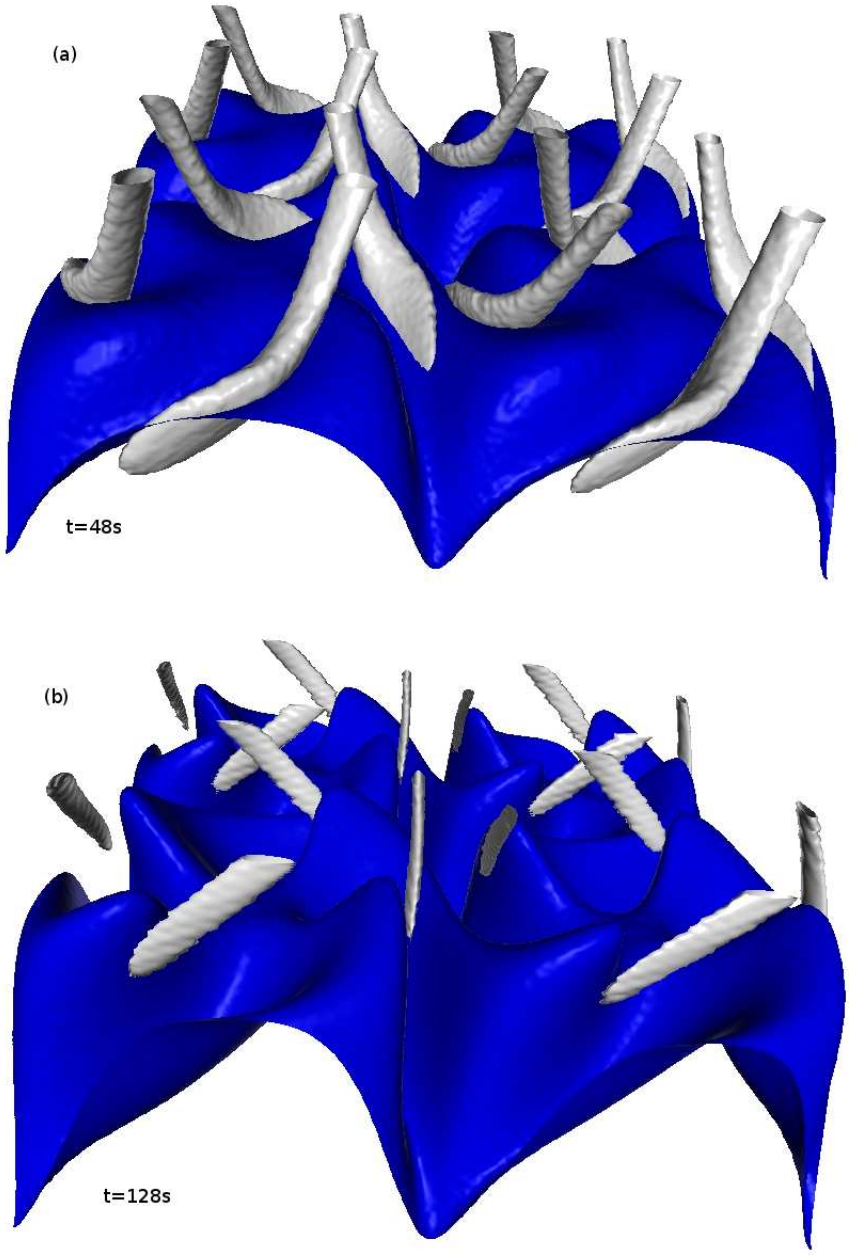

FIG. 11: The Euler surface ϕ_1 (in Blue) at two time instants overlaid with isosurfaces of $\mid \mathbf{H}_1 \mid$ (in Grey). The reduction in intersections between the two isosurfaces along with a concurrent rise in $\mid \mathbf{H}_1 \mid$ is in general agreement with the understanding that magnetic field lines exclude a local region with intense magnetic field.

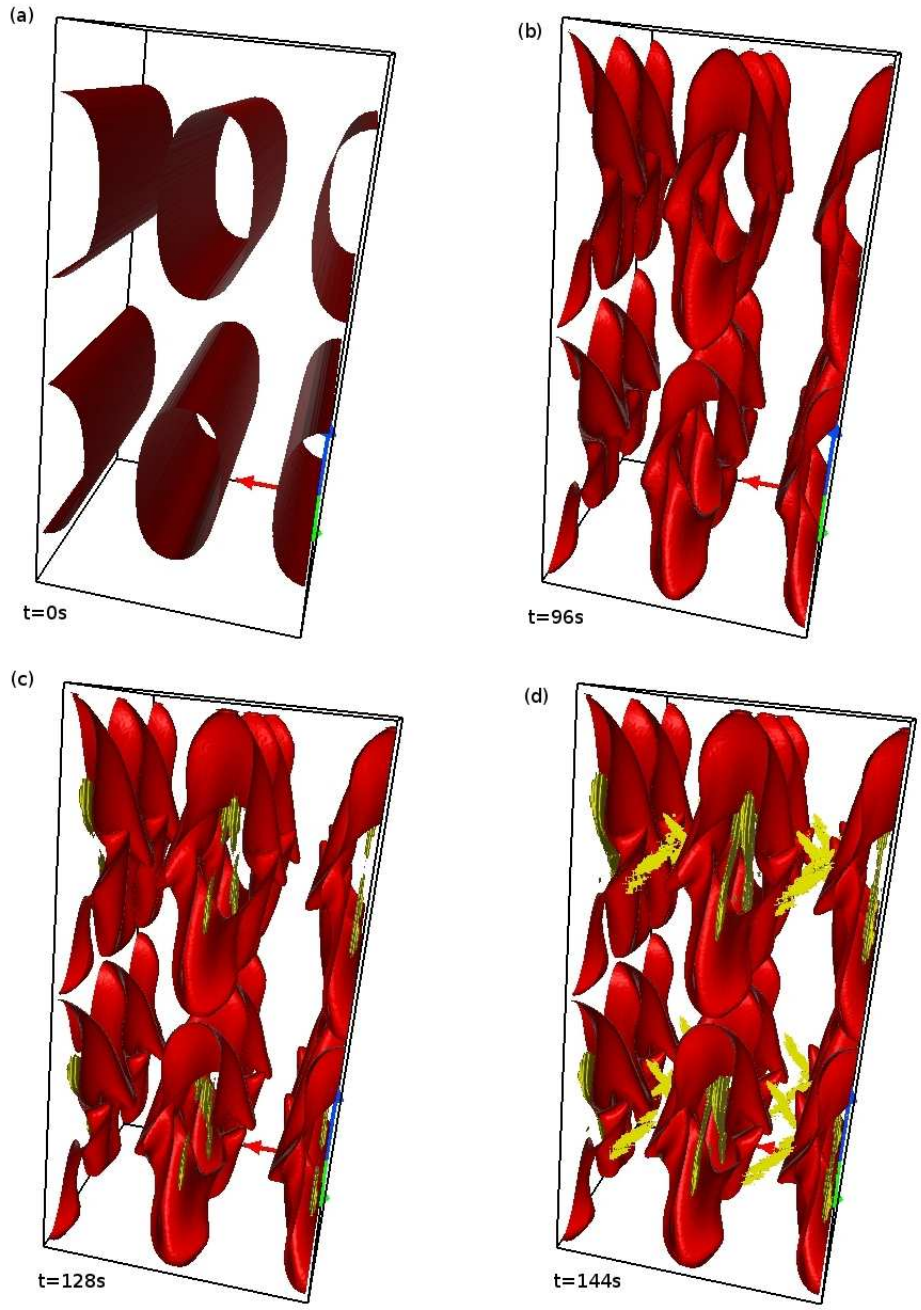

FIG. 12: Evolution of Euler surfaces $\psi_2 = 0.85, -0.85$ (in red), overlaid with $J_2 - 60$ (in yellow). The figure clarifies development of CSs through a squeezing of ψ_2 Euler surface across the O-type null.

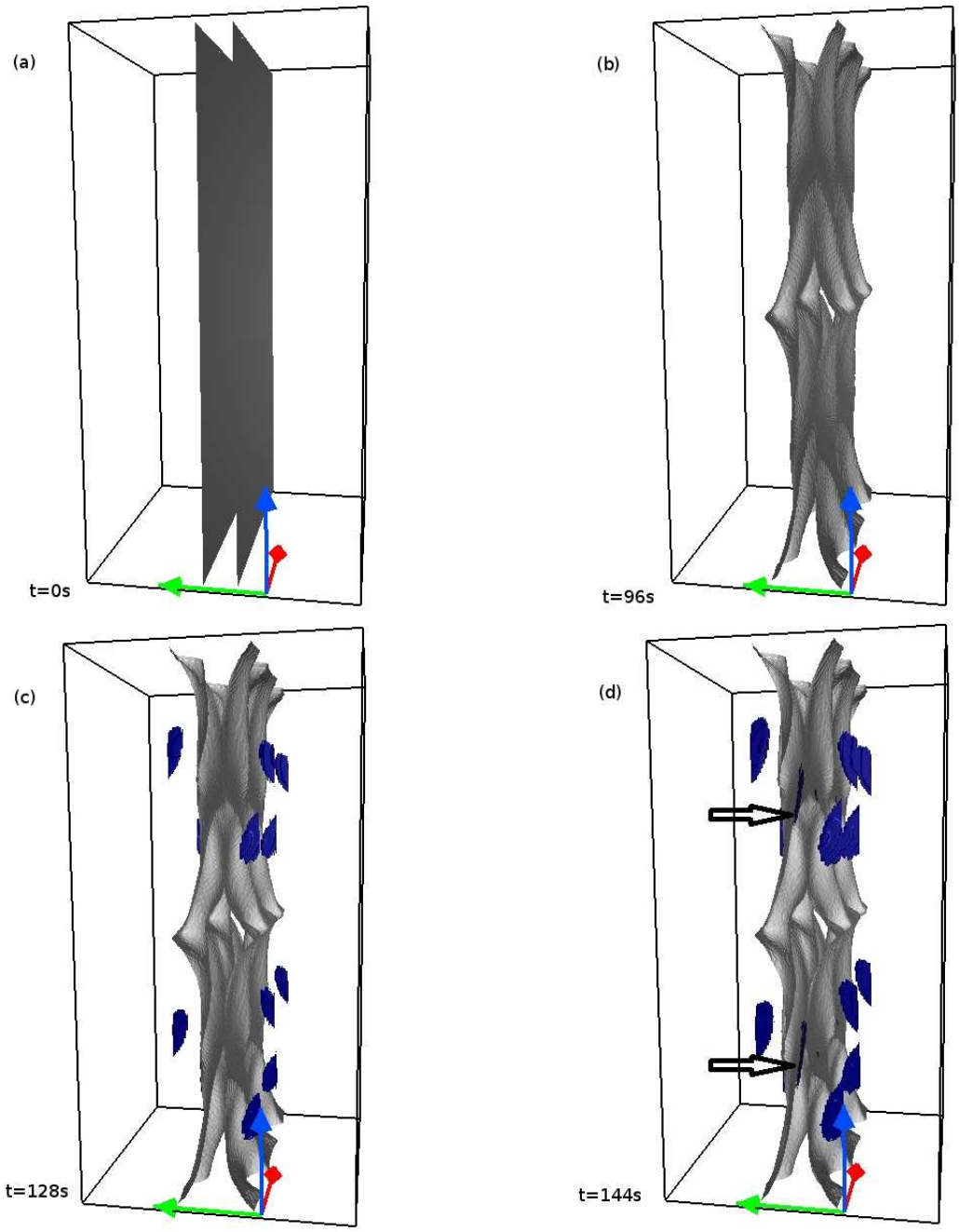

FIG. 13: Time sequence of Euler surfaces $\phi_2 = -0.40$ (in grey), overlaid with $J_2 - 60$ (in blue). The two Euler surfaces depicted in the figure reside on two opposite sides of the field reversal layer. Formation of CSs (marked by arrows) through contortions of ϕ_2 is evident from the figure. A different color scheme in this particular figure is used for a better depiction of CS formation.